ELSEVIER

Alzheimer's & Dementia ■ (2018) 1-20

Alzheimer's & Dementia

Featured Article

Generation of a human induced pluripotent stem cell–based model for tauopathies combining three microtubule-associated protein tau mutations which displays several phenotypes linked to neurodegeneration

Juan Antonio García-León[a,*,1], Alfredo Cabrera-Socorro[b,2], Kristel Eggermont[a,2], Ann Swijsen[d,e], Joke Terryn[a,e], Raheem Fazal[a,d,e], FatemehArefeh Nami[a], Laura Ordovás[a], Ana Quiles[a], Frederic Lluis[a], Lutgarde Serneels[c], Keimpe Wierda[d,e], Annerieke Sierksma[c], Mohamed Kreir[b], Francisco Pestana[b], Philip Van Damme[d,e,f], Bart De Strooper[c,g], Lieven Thorrez[h], Andreas Ebneth[b], Catherine M. Verfaillie[a,d,**]

[a]*Department of Development and Regeneration, Stem Cell Biology and Embryology, KU Leuven Stem Cell Institute, Leuven, Belgium*
[b]*Janssen Research & Development, a Division of Janssen Pharmaceutica N.V., Beerse, Belgium*
[c]*VIB Center for the Biology of Disease, Leuven, Belgium Center for Human Genetics, Universitaire ziekenhuizen and LIND, KU, Leuven, Belgium*
[d]*KU Leuven-Department of Neurosciences, Experimental Neurology and Leuven Research Institute for Neuroscience and Disease (LIND), Leuven, Belgium*
[e]*VIB Center for Brain and Disease Research, Laboratory of Neurobiology, Leuven, Belgium*
[f]*University Hospitals Leuven, Department of Neurology, Leuven, Belgium*
[g]*Institute of Neurology, University College London, London, UK*
[h]*Tissue Engineering Laboratory, Department of Development and Regeneration, KU Leuven, Campus Kulak Kortrijk, Kortrijk, Belgium*

Abstract

Tauopathies are neurodegenerative diseases characterized by TAU protein–related pathology, including frontotemporal dementia and Alzheimer's disease among others. Mutant TAU animal models are available, but none of them faithfully recapitulates human pathology and are not suitable for drug screening. To create a new *in vitro* tauopathy model, we generated a footprint-free triple *MAPT*-mutant human induced pluripotent stem cell line (N279K, P301L, and E10+16 mutations) using clustered regularly interspaced short palindromic repeats-FokI and piggyBac transposase technology. Mutant neurons expressed pathogenic 4R and phosphorylated TAU, endogenously triggered TAU aggregation, and had increased electrophysiological activity. TAU-mutant cells presented deficiencies in neurite outgrowth, aberrant sequence of differentiation to cortical neurons, and a significant activation of stress response pathways. RNA sequencing confirmed stress activation, demonstrated a shift toward GABAergic identity, and an upregulation of neurodegenerative pathways. In summary, we generated a novel *in vitro* human induced pluripotent stem cell TAU-mutant model displaying neurodegenerative disease phenotypes that could be used for disease modeling and drug screening.

Keywords: Tauopathies; Frontotemporal dementia; Parkinsonism linked to chromosome 17; Progressive supranuclear palsy; Alzheimer's disease; CRISPR-Cas; Disease modeling; Drug screening; Neurodegeneration

The authors have declared that no conflict of interest exists.

[1]Current address: Department of Cell Biology, Genetics and Physiology, Faculty of Sciences, Research Biomedical Institute of Malaga (IBIMA), University of Malaga, Campus de Teatinos s/n, 29010 Malaga, Spain. Center for Networked Biomedical Research on Neurodegenerative Diseases (CIBERNED), Madrid, Spain.

[2]These authors contributed equally.

*Corresponding author. Tel.: ■■■; Fax: ■■■.

**Corresponding author. Tel.: ■■■; Fax: ■■■.

E-mail addresses: jgarleon@hotmail.com or juanantonio.garcialeon@kuleuven.be (J.A.G-L.), catherine.verfaillie@kuleuven.be (C.M.V.)

https://doi.org/10.1016/j.jalz.2018.05.007

1. Introduction

Tauopathies are a group of sporadic and familial neurodegenerative disorders, which are characterized by filamentous accumulations of hyperphosphorylated TAU proteins in neurons and glial cells [1]. They are classified into primary or secondary tauopathies depending on whether TAU pathology is the major contributing factor to neurodegeneration or if it is associated with other pathologies. Primary tauopathies include Pick's disease, progressive supranuclear palsy, corticobasal degeneration, argyrophilic grain disease, frontotemporal dementia with parkinsonism linked to chromosome 17 (FTDP-17), globular glial tauopathy, and others. On the other hand, secondary tauopathies represent a rather heterogeneous group of disorders of quite diverse etiology, including Down's syndrome, Lewy body disorders, and, the most prevalent and studied one, Alzheimer's disease (AD). AD represents the most common cause of dementia in the elderly, clinically characterized by a progression from episodic memory problems to a slow global decline of cognitive function that leaves patients with end-stage AD bedridden and dependent on custodial care, with death occurring on average 9 years after diagnosis. Histopathologically, AD is distinguished by the presence of both plaques of β-amyloid and neurofibrillary tangles composed of hyperphosphorylated TAU species, with both pathological hallmarks playing a fundamental role in AD pathology [2].

TAU is a microtubule-stabilizing protein encoded by the microtubule-associated protein TAU (*MAPT*) gene on chromosome 17q21.31 spanning 16 exons, with exons 2, 3, and 10 being alternatively spliced. Differential splicing results in the expression of six different isoforms present in the adult human brain. TAU isoforms differ in the absence or presence of one or two 29 amino acid inserts (0N, 1N, 2N) in the amino-terminal part (encoded by exons 2 and 3) and in the presence of three or four highly conserved repetitive microtubule-binding domains in the C-terminal part (3R or 4R, encoded by exons 9–12) [3]. In both human and mouse fetal brain, only the shorter 3R isoforms are detected, whereas 4R isoforms arise during development, and both isoforms become equally expressed in the adult brain [1]. The developmental switch of incorporating exon 10 in the TAU protein results in the addition of microtubule-binding repeats, which may stabilize microtubules. Accordingly, expression of 3R isoforms in fetal neurons may support their higher plasticity, required for process formation and neurite elongation, during neuronal development. Aberrant regulation of exon 10 splicing in the adult brain has been identified as a major cause of tauopathies, resulting in an imbalance of 3R and 4R TAU isoforms [4].

More than 50 mutations in the *MAPT* gene have been described so far [5]. *MAPT* mutations are typically associated with FTDP-17 but have also been observed for Pick's disease, progressive supranuclear palsy, corticobasal degeneration, and globular glial tauopathies. Phenotypes caused by *MAPT* mutations are heterogeneous, even within family relatives carrying the same mutation(s) [6]. Most mutations are located in exons 9–12 encoding for the repeat regions and adjacent introns and affect either protein levels or the alternative splicing of the pre-mRNA [6]. Several of these mutations cause a decrease in the affinity of TAU for microtubules and a reduced ability to promote microtubule assembly. Other mutations affect exon 10 splicing capacity, resulting in a shift in the physiological ratio between 3R and 4R isoforms [7]. In addition, some mutations facilitate TAU phosphorylation, the main and most diverse post-translational modification of TAU, causing a significant heterogeneity of different TAU molecules. Increased TAU phosphorylation is associated with its aggregation into neurofibrillary tangles in AD and other tauopathies, likely affecting synaptic activity, neuronal physiology, and underlying neurodegeneration [8].

In an attempt to reproduce the pathology present in AD and other tauopathies, numerous animal models have been generated based on the (over)expression of wild-type (WT) or mutant forms of human TAU. Depending on the TAU variant over-expressed and the genetic background of the animal, TAU aggregation and phosphorylation, neuronal and synaptic activity impairments, behavioral deficits, and motor disturbances have been described [9]. With the advent of induced pluripotent stem cell (iPSC) technology, iPSCs have been generated from individuals carrying different *MAPT* mutations and differentiated into neurons. Although different aspects of tauopathy have been reported, findings are heterogeneous, possibly due to the presence of different *MAPT* mutations, in methods used and/or the phenotypic aspects that were evaluated [10–13].

To generate a robust model for tauopathies also suitable for drug discovery screenings, we generated a footprint-free triple *MAPT*-mutant human iPSC line that when differentiated to cortical neurons reproduces several neurodegenerative aspects, including modified TAU isoform expression, TAU aggregation, altered electrophysiological activity, aberrant cortical neuron differentiation, and an activation of pathways related to inflammation, oxidative stress, endoplasmic reticulum/unfolded protein response (ER/UPR), and apoptosis. RNAseq analysis of WT and *MAPT*-mutant cells confirmed these findings and further revealed a shift of differentiation into GABAergic neurons in the mutant cells, as well as an increased expression of pathways previously linked to neurodegeneration.

2. Results

2.1. *Selection of* MAPT *mutations and generation of triple TAU-mutant iPSC lines*

To generate a robust model reproducing different characteristics of tauopathies, we introduced three mutations (N279K, P301L, and E10+16) in and next to exon 10 of the *MAPT* gene in WT donor healthy-derived human iPSCs. The N279K and P301L mutations are among the most

prevalent FTDP-17–linked mutations, causing early onset and aggressive disease progression. These mutations are characterized by the presence of phosphorylated TAU species in both neurons and glia and an elevated prevalence of 4R TAU isoforms [14]. The E10+16 mutation is located in the intron between exons 10 and 11, resulting in an alteration of a stem-loop structure affecting splicing of the pre-mRNA, and increasing incorporation of exon 10 in TAU, thus increasing the expression of 4R TAU isoforms [15]. Together, these three mutations account for up to 60% of all FTDP-17 cases [16].

We used clustered regularly interspaced short palindromic repeats (CRISPR)-FokI nucleases to introduce the mutations, as they are known to cause less off-target effects than the CRISPR-Cas9 system [17]. The donor plasmid used for homology-directed recombination (gently provided by Dr. Kosuke Yusa, Wellcome Trust Sanger Institute, UK [18]) included a positive (hygromycin resistance [HYG^R]) and a negative (thymidine kinase [TK]) selection cassette, with a 3′ homology arm containing the three selected point mutations (Fig. 1A). After HYG selection and clonal expansion, the recombinant clones were evaluated for *in situ* integration (Fig. 1B and C) and presence of the three selected mutations. To excise the HYG/TK selection cassette without any additional modification in the genome, the piggyBac transposase system was used, by using piggyBac inverted terminal repeats flanking the HYG/TK cassette. An endogenous TTAA site was present next to the N279K mutation, allowing the employment of this strategy (Fig. 1A) [18]. Following transient expression of the piggyBac transposase, cells were cultured with 1-(2-deoxy-2-fluoro-1-D-arabinofuranosyl)-5-iodouracil (FIAU) to select for cells from which the TK-containing selection cassette was removed [18] (see Fig. 1 for a scheme about the generation of the mutant cells). This resulted in the generation of heterozygous triple *MAPT*-mutant hiPSCs displaying a pluripotent phenotype (Fig. 1G), which retained their capacity to differentiate into the three germinal layers on embryoid body formation (Fig. 1H). The array comparative genome hybridization analysis confirmed that genome integrity was preserved after CRISPR-FokI treatment (Supplementary Fig. 1).

2.2. Neuronal differentiation and TAU expression

To evaluate the effect of *MAPT* mutations, we differentiated both WT and mutant (triple TAU-mutant) iPSCs to cortical neurons for up to 200 days, using a protocol developed by Shi et al. [19]. We first evaluated the expression of *MAPT* isoforms by qRT-PCR based on the presence/absence of exon 10 (*3R*- vs. *4R-MAPT* isoforms) during differentiation. We observed a significant alteration of the 3R/4R ratio in triple TAU-mutant neurons, as *4R-MAPT* mRNA was already highly expressed in mutant cells on day *in vitro* (DIV) 32 (neural progenitor stage, neural precursor [NPC]). Four repeat-*MAPT* RNA could only be detected from DIV160 onward in WT neurons (Fig. 2A–F), consistent with the notion that 4R-TAU expression is only found in mature neurons. The expression of 4R TAU protein was also confirmed by Western blotting (Fig. 2G).

On DIV65 and DIV94, we assessed the protein levels of total TAU and phosphorylated TAU isoforms by Western blotting. As shown in Fig. 2H–J, more total and phosphorylated TAU isoforms (determined by the use of the AT270 and AT8 antibodies) protein was present at both time points. We also assessed the presence of detergent-insoluble TAU isoforms, finding little if any presence of insoluble TAU isoforms within the mutant neurons (data not shown).

As expression of aberrant TAU isoforms has been reported to cause TAU disassembly and accumulation in neuronal soma [14], we assessed TAU distribution within neuronal cells by visualization of total TAU by confocal microscopy. As can be clearly observed (Fig. 2K), differential pattern of TAU distribution was seen between WT and mutant neurons. In WT cells, TAU was homogeneously distributed along neuronal prolongations, whereas in mutant neurons, TAU was clearly more concentrated within the cell soma, consistent with an abnormal physiology in the maintenance and/or functioning of TAU in the mutant neurons.

2.3. TAU aggregation

We next explored the aggregation potential of TAU in the triple mutant-TAU neurons by amplified luminescent proximity homogeneous assay (alpha-LISA technology). The assay uses antibodies recognizing human TAU (hTAU10) and labeled with either a donor or acceptor bead. When TAU proteins are aggregated, the proximity of the donor- and acceptor-labeled antibodies leads to the emission of light at 615 nm. The assay hence allows the quantitative detection of aggregated TAU (hTAU10/hTAU10 signal) in a high-throughput-compatible setting [20].

As we previously reported [20], in WT neurons, no TAU aggregation can be observed unless the cells are transduced with an adeno-associated viral vector encoding P301L mutant TAU and are simultaneously seeded with K18 (aggregates of recombinant 4R TAU produced *in vitro*). K18 triggers aggregation of overexpressed but not endogenously produced TAU in control cells, which was used as a positive control in our assays. Similarly, WT cells did not show an increase in hTAU10/hTAU10 signal when only seeded or transduced. In contrast, we observed a twofold increase in hTAU10/hTAU10 signal in triple TAU-mutant neurons following either P301L transduction or K18 seeding separately (Fig. 2L and M). Interestingly, we quantified a 15-fold increase in hTAU10/hTAU10 signal when P301L was overexpressed in TAU-mutant neurons on DIV60, increasing up to 50-fold 10 days later (DIV70, Fig. 2L). We also evaluated if aggregated TAU was also phosphorylated in mutant neurons by quantifying AT8 detection using AlphaLISA. The signal for $AT8^+$/phosphorylated TAU in untreated or seeded cells with K18 was significantly higher in mutant

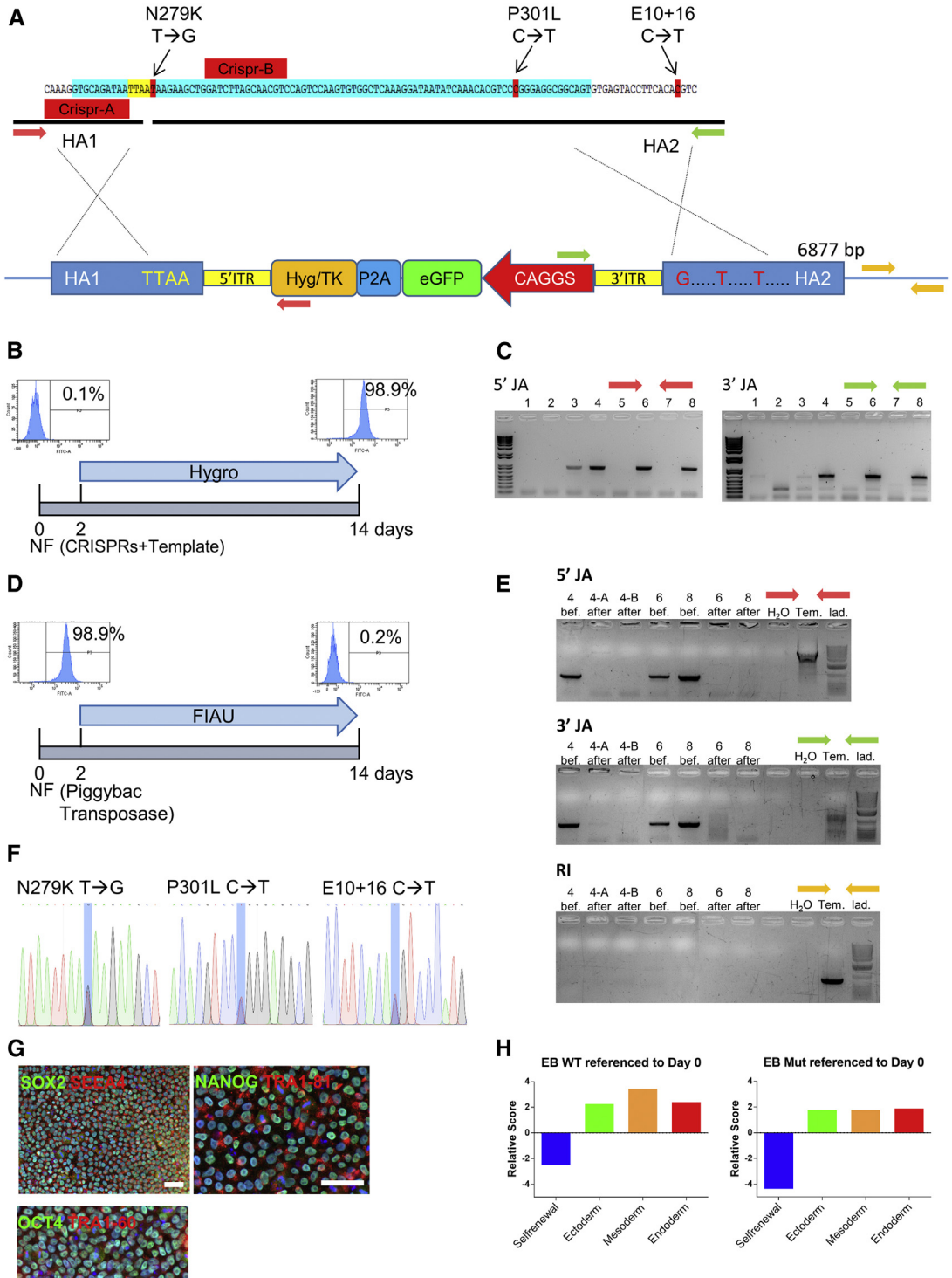

Fig. 1. Design and generation of the triple TAU-mutant hiPSC lines. (A) General overview of the experimental design and strategy used to generate the template DNA including the double selection cassette and the introduction of the selected mutations into the genome through direct genome targeting mediated by tailored CRISPR-FokI nucleases and homologous recombination (HR) between highly similar sequences. (B) Layout of the nucleofection (NF) with CRISPR-FokI nucleases plus template DNA and HYG selection to generate iPSC clones harboring the GFP^{+} selection cassette. (C) Example of junction assay (JA) PCRs to discriminate the presence or absence of the selection cassette in the *MAPT* gene in different clones. (D) Experimental design for excision of selection cassette by NF of the piggyBac Transposase followed by FIAU negative selection. (E) JA PCRs demonstrating correct integration of the selection cassette before and after the excision of the piggyBac Transposase; and random integration (RI) PCRs demonstrating absence of random cassette integration in the genome. (F) Sequencing of the *MAPT* gene following genetic modification demonstrating presence of the three mutations in heterozygosity. (G) *MAPT*-mutant hiPSCs express typical pluripotency markers as SOX2, SEEA4, NANOG, TRA1-81, OCT4, and TRA1-60. Hoechst 33258 (blue) was used as nuclear marker. Scale bars: 50 μm. (H) Results of embryoid body formation and characterization using the score card assay (three germ layer differentiation and loss of pluripotency marker gene expression). Abbreviations: bef., before; Tem., template; lad., ladder.

neurons (Fig. 2N), suggesting that TAU aggregates detected are also hyperphosphorylated, similar to the neurofibrillary tangles found in AD affected brains [3]. Overall, these studies indicate that endogenously expressed triple mutant-TAU may be sufficient to seed for TAU aggregation *in vitro*.

2.4. Triple TAU-mutant neuronal progeny displays increased electrophysiological activity

Patient iPSC-derived neurons with *MAPT* mutations affecting exon 10 splicing have been previously described to display a faster maturation phenotype as defined by their electrophysiological properties [21]. We hypothesized that this phenotype would also be reproduced in the triple mutant-TAU iPSC progeny. We applied whole-cell patch-clamp on iPSC-derived neurons to record action potentials and voltage-gated currents on an early (DIV70) and a late (>DIV90) stage during neuronal differentiation. At both time points, WT and TAU-mutant cells displayed a comparable percentage of cells firing spontaneous (Fig. 3D and F) and evoked (Fig. 3E and G) action potentials. Quantification of the number of spontaneous (Fig. 3H and J) and evoked (Fig. 3I and K) action potentials revealed a similar firing frequency between WT and TAU-mutant cells on DIV70 and on >DIV90. TAU-mutant neurons displayed slightly decreased inward and outward voltage-gated current densities compared with WT neurons on DIV70 ($P < .05$; Fig. 3L and M), whereas no differences were observed at >DIV90 (Fig. 3N and O).

Basic electrophysiological membrane properties (capacitance and potential) were similar in WT and TAU-mutant cells on DIV70 and >DIV90, except that the membrane potential on >DIV90 was more depolarized in TAU-mutant than that in WT cells (WT: -55 ± 2 mV, mutants: -48 ± 2 mV; $P = .0172$).

To exclude the intrinsic bias associated with single-cell patch-clamping, wherein only a limited number of individual cells are evaluated and without considering the overall neuronal network activity, we assessed electrophysiological properties of the neurons using multielectrode arrays (MEAs). Co-culture of iPSC-derived neurons with murine primary astrocytes (1:1 ratio) was used, as this hastens electrophysiological maturation of iPSC neurons [22]. MEAs provide information on the electrical properties of the whole neuronal population by measuring extracellular potentials across electrodes distributed throughout the culture wells. Using this experimental setup, we observed a significant increase in the number of spikes, bursts, and burst frequency in triple TAU-mutant neurons compared with WTs (on DIV60, Fig. 3P–S), suggesting an increase in the electric activity due to the TAU mutations.

2.5. Aberrant differentiation of TAU-mutant iPSCs to cortical neurons

We next assessed if presence of the three *MAPT* mutations affected the differentiation of iPSC toward cortical neurons. We analyzed neurons at different time points for expression of cortical layer markers both at the mRNA and protein levels (Fig. 4). As shown in Fig. 4A–L, early during differentiation (DIV32–45), mutant cells displayed increased levels of early neuronal and deeper cortical layer markers, including FOXG1, CTIP2, and BRN2 compared with WT cells, suggesting an accelerated maturation of mutant cells. By contrast, mutant cells expressed lower levels of transcripts and/or proteins of markers for superficial layer cortical neurons, such as SATB2, while these levels progressively increased from DIV65 onward during the differentiation of WT cells. A similar trend was observed for TBR1 (Fig. 4C), which in addition to be a marker for deep cortical layers, also plays a role in glutamatergic projection and, therefore, in the development of cortical layers [23]. Differences in cell proliferation (EdU^+ cells) were observed as well between WT and mutant cells, with a higher prevalence of EdU^+ WT neurons at early time points (DIV40) but a greater number of EdU^+ TAU-mutant neurons later (DIV68, Fig. 4M).

To further address the impact of the triple *MAPT* mutations on the neuronal progeny, we performed RNAseq analysis on WT and mutant iPSC neuronal progeny harvested on DIV70 and DIV110. Unsupervised principal component analysis demonstrated that WT and triple TAU-mutant neurons, at both time points, clustered separately (Fig. 5A). 1490 (DIV70) and 1868 (DIV110) genes were differentially expressed between both genotypes (adjusted P-value $< .05$ & log twofold change), 395 of which were shared for both time points (Fig. 5B). We next analyzed the different cell populations using a set of markers that define different neuronal populations, developmental stages, and different forebrain areas [24]. This demonstrated that, as expected, DIV70 and DIV110 progeny clustered together, with a clear distinction between WT and mutant progeny at both time points (Fig. 5C). Further analysis also demonstrated that expression of typical glutamatergic and GABAergic marker genes was significantly different. Mutant cells expressed lower levels of glutamatergic markers and increased levels of GABAergic markers compared with WT cells, differences that were more pronounced on DIV110 (Fig. 5D). This was further substantiated by ingenuity pathway analysis, demonstrating significantly lower expression of glutamatergic signaling pathway as well as genes involved in synaptic long-term potentiation (LTP) in TAU-mutant neurons (Fig. 5E and F).

As differences in the balance between excitatory and inhibitory transcripts were observed at the transcriptome level between WT and triple TAU-mutant cells, we immunostained DIV88 progeny with antibodies against the glutamate (excitatory) and GABA and glycine (inhibitory) neurotransmitter transporters, vGlut1 and vGat, respectively. Quantification was performed based on the intensity thresholds and normalized to the number of $DAPI^+$ nuclei or the expression of the neuronal marker β-3-tubulin (Supplementary Fig. 2A–F). The area and integrated density

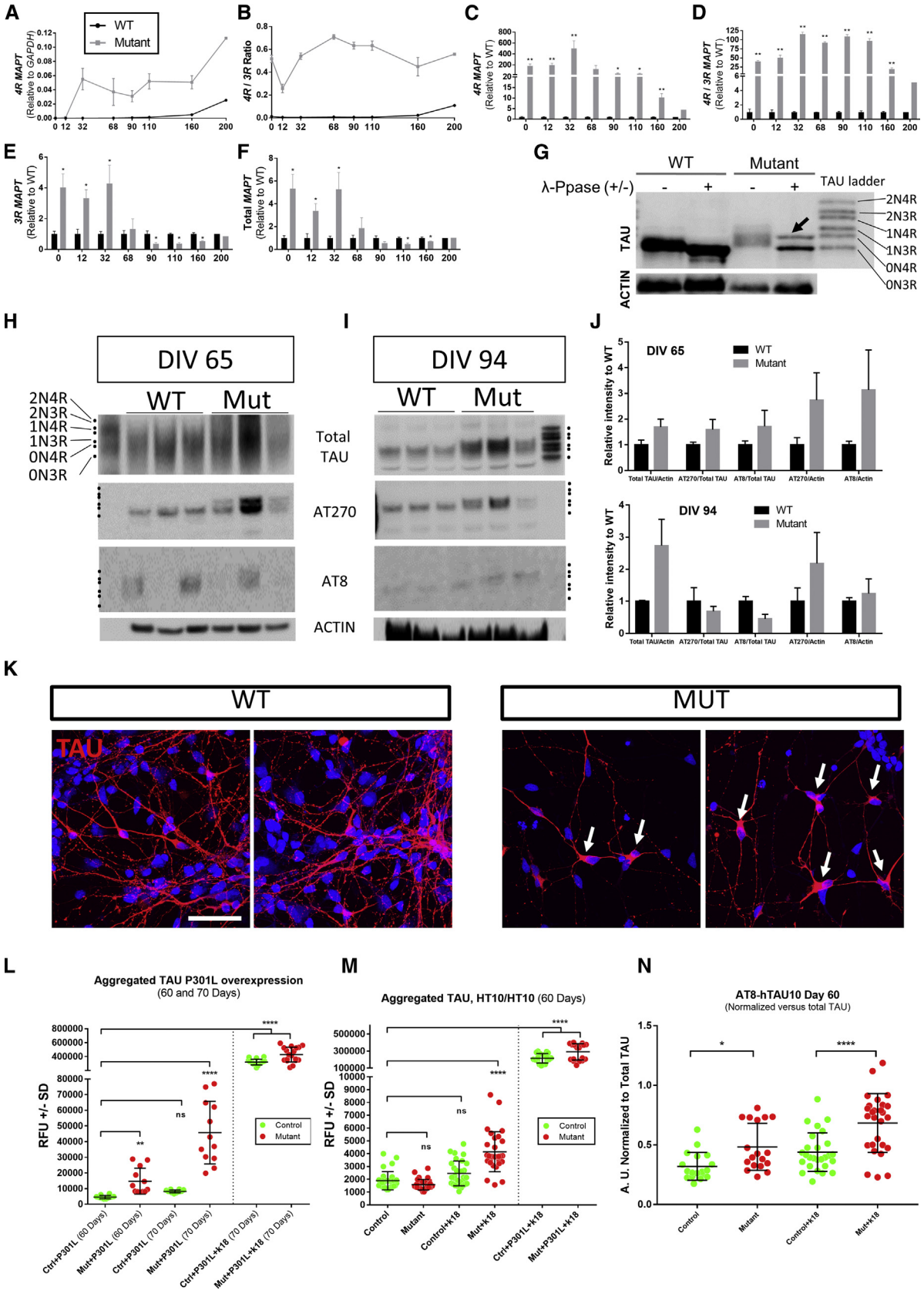

Fig. 2. Increased 4R TAU expression and TAU aggregation in the triple-mutant TAU cortical neurons. (A–F) qRT-PCR analysis showing expression of 3R and Q14 4R TAU isoforms during the neuronal differentiation of both WT and triple TAU-mutant cells. (A) Relative expression to glyceraldehyde 3-phosphate

(product of the area by the intensity) of vGat-positive staining related to the number of nuclei was higher in TAU-mutant cells than in WT cells (even if this did not reach statistical significance, Supplementary Fig. 2B and C). Nevertheless, when we compared the area of vGat-positive staining to the total area of β-3-tubulin, these differences were not obvious, with presence of ±40% of positive area for both vGlut and vGat markers referred to the β-3-tubulin positive area. This suggests that it may be necessary to analyze many more markers for excitatory vs. inhibitory neurons and that single marker analysis might not reveal the differences present between WT and mutant cultures.

We also evaluated the presence of $GFAP^+$ cells in the cultures (Supplementary Fig. 2E–G). On DIV65, 12.01 ± 1.82% of the cells present in the culture expressed the GFAP antigen, consistent with previous reports [19]. Subtle differences were found in the percentage of $GFAP^+$ cells between WT and mutant cells (WT: 9.05 ± 2.29% vs. mutant: 14.97 ± 1.61% of $GFAP^+$ cells), but this did not reach statistical significance. Notably, most of these $GFAP^+$ cells (82.19 ± 5.23% in total) presented a bipolar elongated phenotype, which would resemble radial-glial–like cells, present in the developing brain [25].

2.6. Mutant cells display a stress gene signature

Several reports indicated the presence of mitochondrial and ER/UPR stress in *MAPT* mutant iPSC-derived neurons and in neurons from tauopathy mouse models and patients [26]. As we observed a progressive cell loss in mutant neuronal cultures compared with WT, we evaluated the RNAseq data to determine if different stress pathways were more highly expressed in triple TAU-mutant progeny compared with WT cells. Gene ontology pathway analysis revealed increased expression of gene ontology terms associated with cellular stress as, for example, "response to interferon-γ", "positive regulation of reactive oxygen species metabolic process", "regulation of extrinsic apoptotic signaling pathway", "activation of signaling protein activity involved in unfolded protein response," and "positive regulation of NFkB signaling", in triple TAU-mutant cells compared with WT progeny at both time points analyzed (DIV70 and 110, Supplementary Tables 1 and 2). Ingenuity pathway analysis performed on selected pathways also demonstrated increased expression of the genes involved in these pathways in mutant cells, as exemplified by the NFkB signaling pathway, represented in Fig. 6Q. The increased activation of stress pathway genes within the TAU-mutant neurons was confirmed by qRT-PCR for marker genes of the oxidative stress, ER/UPR stress, and inflammatory response pathways, on different time-points throughout neuronal differentiation (Fig. 6A–M). This was confirmed at the protein level because the expression of the tumor necrosis factor receptor 1 (implicated in inflammatory response) and CHOP (involved in ER/UPR) was significantly upregulated within the mutant neurons (Fig. 6N–P).

In addition, to substantiate the observation that triple TAU-mutant progeny were progressively lost from culture over time, we assessed the frequency of apoptotic cells in culture. We observed significantly more $CASPASE3^+$ neurons in the triple TAU-mutant iPSC progeny compared with WT (Fig. 6R and S). Moreover, apoptotic nuclei (characterized by a reduction of nuclear size and compaction of genomic material) were also frequently observed at the beginning of neuronal maturation (∼DIV40), but this only in triple TAU-mutant progeny (Fig. 6T and U). Thus, triple TAU-mutant neuronal progeny, at least under these culture conditions, suffered from oxidative, protein folding, and inflammatory stress, which might underlie the increase for apoptosis.

2.7. Neurite outgrowth

TAU is a microtubule-stabilizing protein implicated in neurite formation, stabilization, and maintenance, as part of its cytoskeletal plasticity functions [26]. Because the *MAPT* mutations altered the ratio between 3R- and 4R-TAU isoforms (Fig. 2), we hypothesized that differences in neurite formation and outgrowth might be present between WT and

dehydrogenase (*GAPDH*) of 4R *MAPT* isoforms during the differentiation of WT (black) and triple TAU-mutant (Mut, gray) neurons. (B) 4R/3R *MAPT* isoform expression ratio during differentiation of both cell types. (C) 4R *MAPT* isoform expression levels during differentiation of TAU-mutant cells relative to WT neurons. (D) 4R/3R *MAPT* isoform ratio expression levels during differentiation of TAU mutant cells relative to WT neurons. (E) 3R *MAPT* isoform expression levels during differentiation of TAU mutant cells relative to WT neurons. (F) Total *MAPT* expression levels during differentiation of TAU mutant cells relative to WT neurons. Data are represented as mean ± standard error of mean (SEM) of N = 3–4 independent experiments. $*P < .05$, $**P < .01$. (G) Western blot analysis for total TAU expression in WT and triple TAU mutant neurons following incubation with or without λ-phosphatase (+/−), demonstrating the presence of 4R TAU expression only in mutant cells (arrow). (H–J) Western blot analysis of total TAU (HT7 antibody) and phosphorylated forms (AT270 and AT8 antibodies) of protein extracts from WT and mutant neuronal progeny on DIV 65 (H) and DIV 94 (I), quantified based on intensity signal in (J). Data are represented as mean ± SEM of N = 3 independent experiments. (K) Immunocytochemistry showing cellular localization of TAU expression (HT7 antibody) in WT and mutant neurons on DIV65. Hoechst 33258 (blue) was used as nuclear marker. Scale bar: 50 μm. (L) hTAU10/hTAU10 alphaLISA values on DIV60 measured in both WT and triple TAU-mutant neuronal progeny in nontreated neurons, in neurons cultivated in the presence of the K18 seed and in neurons cultivated in the presence of the K18 seed and transduced to overexpress the P301L mutant TAU. Cells that were seeded and transduced were used as a positive control. (I) hTAU10/hTAU10 alphaLISA values measured in both WT and triple TAU-mutant transduced neurons without the presence of the K18 seeding on DIV60 and DIV70, and alphaLISA levels measured on DIV70 in both cell types transduced and in the presence of the K18 seeds. (N) AT8/hTAU10 alphaLISA values referred to phosphorylated TAU aggregation from WT and mutant cells seeded in the absence or presence of the K18 seed. N = 3–6 independent replicates, One-way analysis of variance. $*P < .05$, $**P < .01$, $****P < .0001$ (Dunnett's multiple comparison test vs. nonseeded control). Abbreviations: RFU, relative fluorescence units; A.U., arbitrary units.

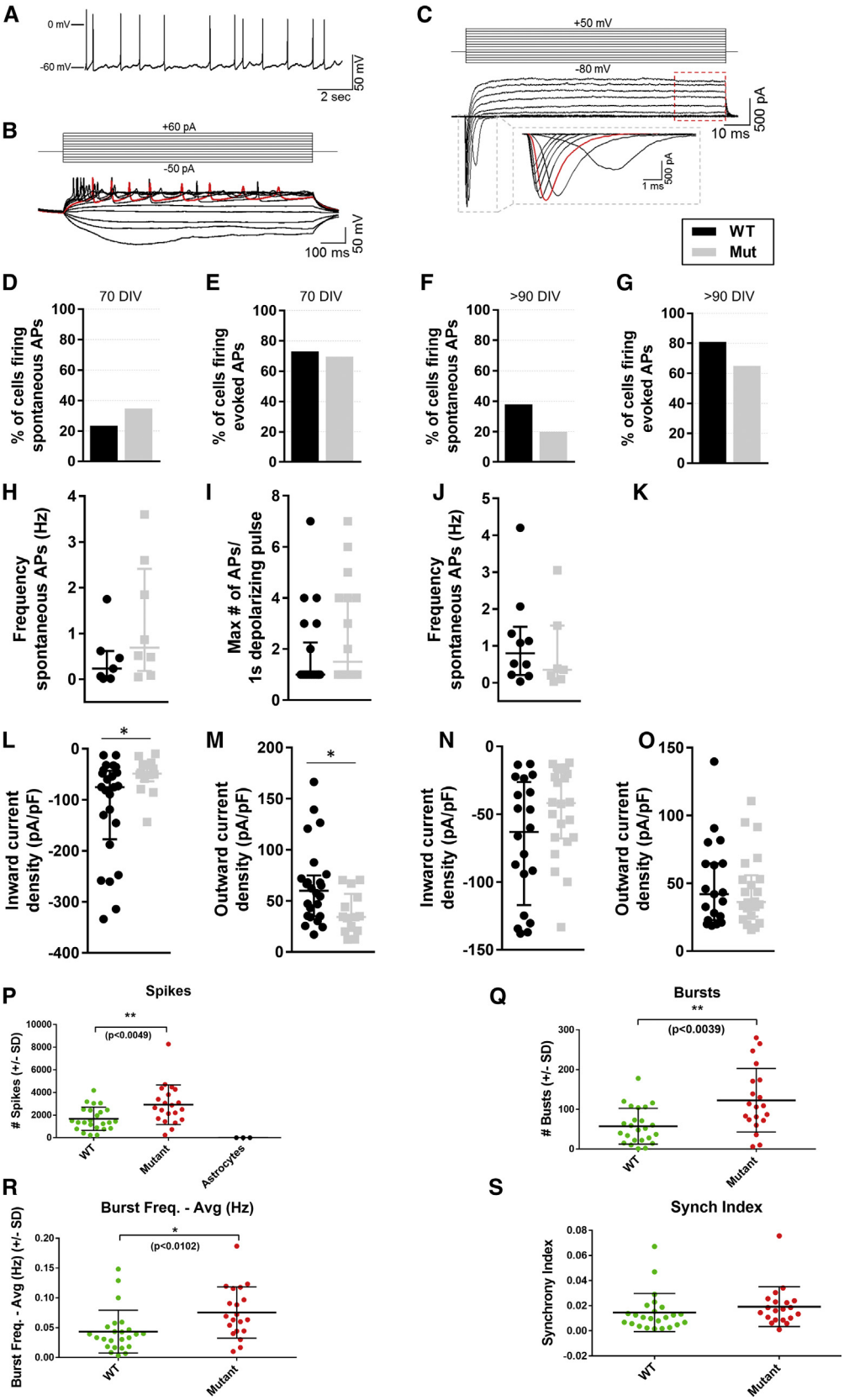

Fig. 3. Altered electrophysiological activity of TAU-mutant iPSC-derived cortical neurons. (A) Representative recording (WT neuron on DIV70) of spontaneous action potentials. No current injection was applied. (B) Experimental current pulse step protocol (top panel) and representative traces (triple TAU-mutant neuron at >DIV90) of membrane potential responses to current injections (lower panel). The membrane potential was clamped at approximately

web 4C/FPO

triple TAU-mutant neuronal progeny (Supplementary Fig. 3). Progeny from WT and TAU-mutant iPSCs on DIV40 were plated and allowed to extend neurites for 3 days before fixation. We used high-content imaging to assess cell morphology and neurite frequency and length following staining with anti-TUJI antibodies.

Compared with WT iPSC progeny, significantly fewer TAU-mutant neurons displayed a multi-branching phenotype, with most of TAU-mutant cells having a bi-polar morphology (Supplementary Fig. 3H and I). We found an almost 50% reduction in the number of branching points in the mutant compared with WT cells (Supplementary Fig. 3B). We also found a reduction in the total area covered by neurites, the total neurite length, and the length of all neurites per cell (Supplementary Fig. 3C–E) in mutant compared with WT cells, even if the cell density was the same in both cultures (Supplementary Fig. 3G). On the other hand, the length of each neurite branch was slightly increased in mutant cells (Supplementary Fig. 3F).

2.8. Confirmation of phenotypic features in a second independent triple TAU-mutant cell line

We evaluated if the findings obtained for the triple mutant-TAU neurons could be reproduced using a second and independently generated genome-engineered line. This independent mutant line reproduced the features displayed by the first mutant line, including increased expression of *4R-TAU* isoforms already on DIV32 (altering therefore the 3R/4R ratio; Supplementary Fig. 4). Action potential proportions and frequencies obtained from the second independent mutant line on DIV70 were also similar to the action potential properties of the first mutant line (Supplementary Fig. 5A–F). The second independently generated triple TAU-mutant line also showed altered cortical marker expression (by qRT-PCR and immunostaining) similar to the data from the first line (Supplementary Figs. 6 and 7); a significant increased expression of genes within the oxidative stress, ER/UPR and inflammatory pathways and a higher prevalence of apoptotic cells (Supplementary Fig. 7); and aberrant neurite outgrowth (Supplementary Fig. 8).

These results confirm that the phenotypic changes identified in the mutant cells are specific for the *MAPT* mutations introduced and are not restricted to cell clone-specific effects.

3. Discussion

Tauopathies are a heterogeneous group of diseases characterized by hyperphosphorylation and accumulation of TAU protein in the brain. Some of these diseases are directly linked to specific *MAPT* gene mutations that alter the physiological ratio between 3R- and 4R-TAU isoforms and/or renders TAU protein more susceptible to aggregation. Nevertheless, the mechanisms underlying TAU-mediated neurodegeneration are only partially understood [27].

Although mouse models have been generated (over)expressing different human TAU variants, these only partially reproduce human TAU pathology with significant variability between models depending on the TAU variant expressed and/or promoter used [9]. In addition, murine neurons appear to be less sensitive to neurodegeneration compared with human neurons [28].

The advent of human iPSCs has created the possibility to study mutations in human cell models. A number of studies have generated iPSC-derived cells from individuals carrying different *MAPT* mutations. These *in vitro* models reproduce some aspects of tauopathies, including the presence of altered TAU isoforms expression, TAU hyperphosphorylation, activation of ER/UPR stress pathways, accelerated electrophysiological maturation, and/or impaired neurite outgrowth [10–13,21]. However, depending on the lines studied, some but not all of these phenotypes were described simultaneously.

Ideally, drug discovery and validation platforms should use cell models wherein most of these TAU-associated phenotypes are present and can be compared with WT control lines, to prove the causal relation of the phenotype. We therefore created an iPSC-derived model that reproduces most of the phenotypes described elsewhere by introducing the three mutations found in >60% FTDP-17 patients (N279K, P301L, and E10+16) [16] in a single iPSC line.

We introduced the three mutations in a footprint-free manner in hiPSCs, combining the CRISPR-FokI

−65 mV between current pulses. The maximal amount of action potentials (red trace) in response to a depolarizing current pulse was counted for every cell. (C) Experimental voltage pulse step protocol (top panel) and representative traces (WT neuron on DIV70) of current responses showing voltage-activated inward and outward currents. The amplitude of the peak inward current (red trace in gray dashed box) was determined for every cell. Outward peak currents were quantified at +30 mV during the time course indicated by the red dashed box. The percentage of WT and TAU-mutant neurons firing spontaneous (D and F) and evoked (E and G) action potentials is similar, on DIV70 (WT: n = 30; mutant: n = 23) as well as on >90 DIV (WT: n = 26; Mutant: n = 35). Firing frequency of spontaneous (H and J) and evoked (I and K) action potentials is comparable in WT and TAU-mutant neurons, on DIV70 (spontaneous, WT: n = 7; Q16 mutant: n = 8; evoked, WT: n = 10, mutant: n = 7) as well as on DIV90 (spontaneous, WT: n = 22, mutant: n = 16; evoked, WT: n = 21, mutant: n = 22). Inward and outward current densities are different between WT (n = 24) and TAU-mutant (n = 14) neurons on DIV70 ($P < .05$; L and M), whereas they were similar on DIV90 (N and O; inward, WT: n = 20, Mut: n = 22; outward, WT: n = 19; Mut: n = 22). The number of patched cells is represented by n; all cells were sampled from four neuronal differentiations. Data are represented as median with interquartile range. Statistical analysis was performed using a Mann-Whitney test. *$P < .05$. (P–S) Electrophysiological activity measured by multi-electrode arrays (MEAs) on DIV65 neural progeny co-cultured with primary astrocytes from DIV40. (P) Depicts the number of spikes (note that astrocytes cultured alone do not display any activity). Q and R show the number of bursts (>5 spikes per second) and burst frequency detected. (S) Depicts synchronicity. N = 3 independent replicates. All data are means ± SD, *t* test. *$P < .05$, **$P < .01$.

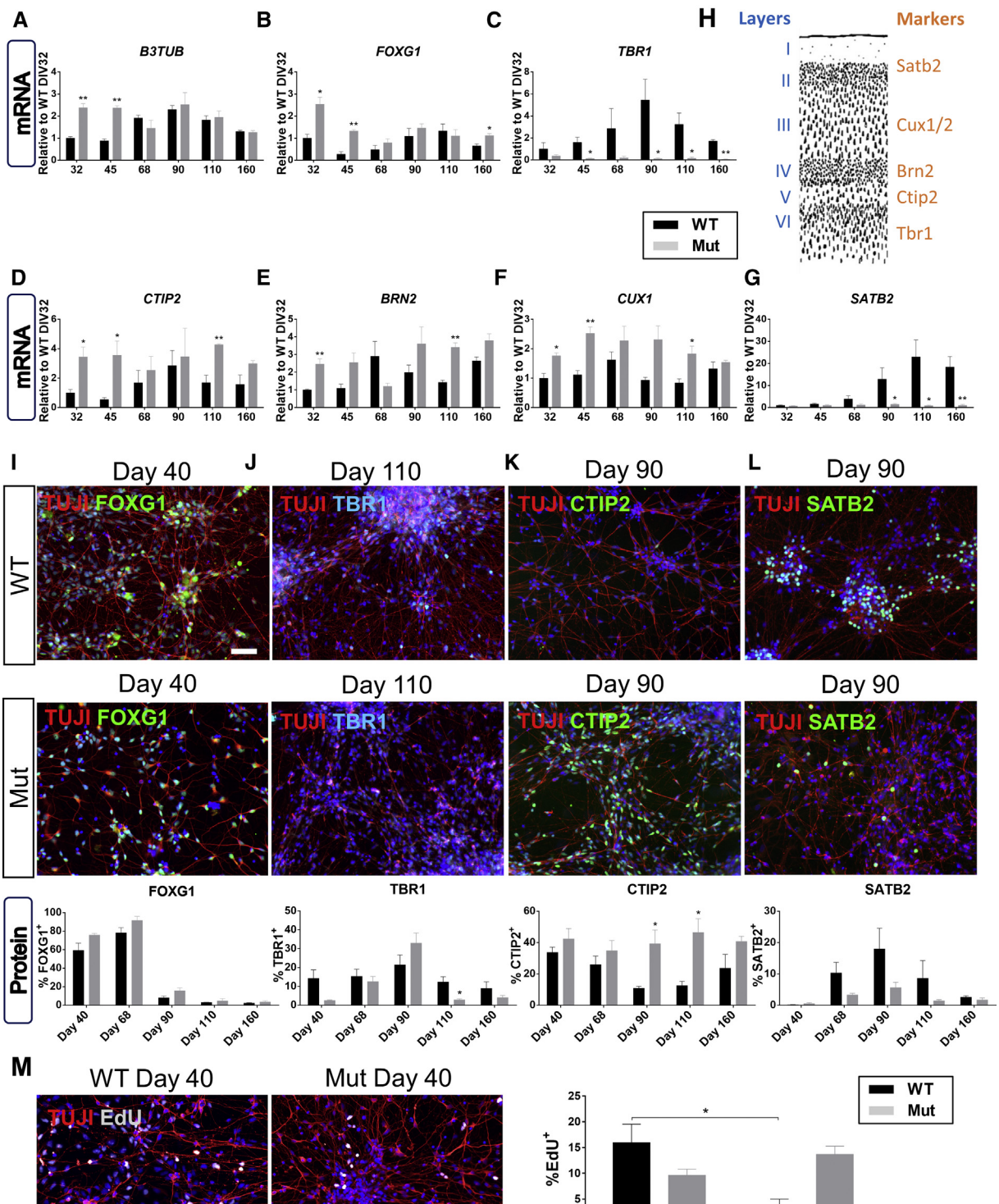

Fig. 4. Altered cortical neuron differentiation from TAU-mutant iPSCs. (A–G) qRT-PCR analysis for deep and superficial cortical layer neuron marker gene expression during differentiation of WT (black) and TAU-mutant iPSC (gray) progeny (*B3TUB*, *FOXG1*, *TBR1*, *CTIP2*, *BRN2*, *CUX1*, and *SATB2*). Gene expression levels are shown as fold changes relative to WT NPCs from DIV32 (gene expression was normalized to the housekeeping gene *GAPDH*). (H) Graphical representation of different cortical layer marker genes. (I–L) Representative pictures for immunostaining of TUJ1 together with FOXG1, TBR1, CITP2, and SATB2 in WT (upper row) and TAU-mutant progeny at the specified time points (middle row). Quantification levels of each marker during differentiation for both cell types (WT in black and TAU-mutants in gray) depicted in the lower row. (M) DIV40 and DIV68 differentiating cells were incubated with EdU for 3 hours, 24 hours before fixation, followed by staining with an antibody against EdU and TUJ1. A representative picture of both WT and TAU-mutant neuronal progeny on DIV40 is shown, with quantification of the percentages of EdU^+ cells at both time points of WT (black) and TAU-mutant cells (gray). Hoechst 33258 (blue) was used as nuclear marker. Scale bar: 50 μm. Data are represented as mean ± SEM of N = 3–4 independent experiments. *$P < .05$, **$P < .01$.

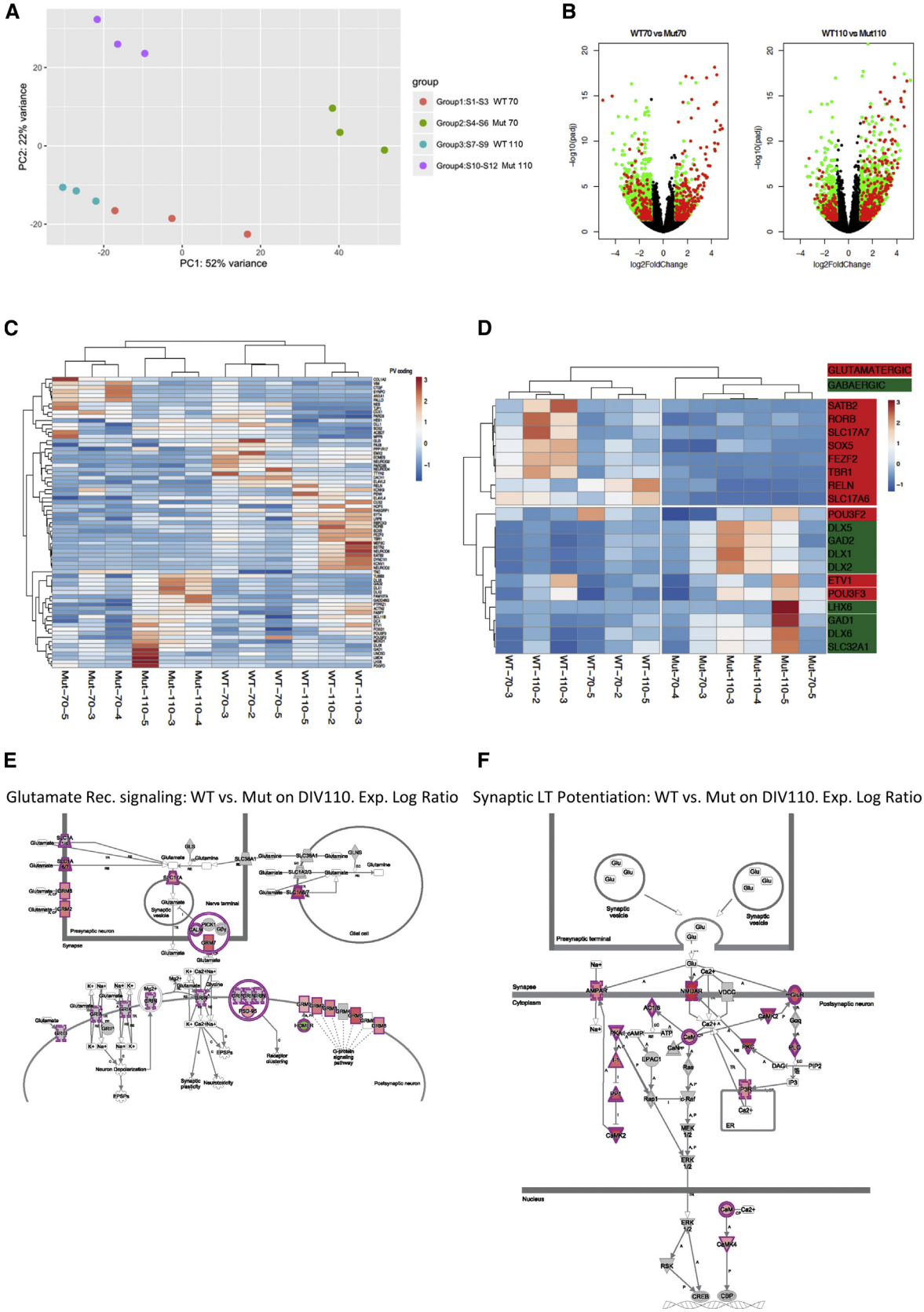

web 4C/FPO

Fig. 5. Genome-wide transcriptome studies demonstrate significant differences between triple TAU-mutant and WT neurons. RNA sequencing (seq) was performed on WT and TAU-mutant iPSC progeny on DIV70 and DIV110. (A) Principal component analysis (PCA) of WT and TAU-mutant iPSC progeny on DIV70 and DIV110. (B) Volcano plots at DIV70 (left) and DIV110 (right) illustrating the number of differentially expressed genes (adjusted P-value $< .05$

nuclease–mediated homology-directed recombination with the piggyBac transposase–mediated excision of a selectable cassette, introduced during the homology–directed recombination [18]. Because of the use of two guide RNAs, this approach has been shown to cause less off-target cuts compared with the CRISPR-Cas9 system [17].

We describe that knock-in of the three mutations in the *MAPT* gene resulted in an altered 3R/4R-TAU isoform expression, with high levels of 4R-TAU already found as early as DIV32 in iPSC neural progeny. The precise knock-in strategy used, together with the observation of similar phenotypes in two independently generated lines, demonstrates conclusively that the *MAPT*-mutations are responsible for this observation.

The three introduced mutations have been reported (individually) to lead to the incorporation of the exon 10 in the mRNA (leading to the expression of 4R-TAU isoforms) and/or expression of pathogenic TAU. Because single or combinations of dual mutation insertions have not been performed, we cannot firmly state which of the mutations is responsible for the phenotypes observed. Nonetheless, due to the wide range of phenotypes, we describe encompassing most of the phenotypes observed by other studies using single TAU-mutated neurons [10–13,21], we hypothesize that the phenotypes we obtained are the consequence of both the incorporation of 4R-TAU isoforms and the synergistic association of the different mutations introduced.

Expression of TAU protein isoforms is brain region and developmental stage-specific [29]. During fetal development, only 3R-TAU isoforms are present, which is believed to be important to allow dynamic changes in neurites and synapses formation. Continued presence of 3R-TAU in postnatal neurons is likely required for the establishment of new synapses [29]. By contrast, 4R-TAU, which binds microtubules with higher affinity than 3R-TAU, become expressed in postnatal cortex [29]. The altered ratio between the two groups of TAU isoforms in the triple mutant neurons may be responsible for the aberrant neurite outgrowth we observed. As the assay can be done using a (semi)-automatic imaging platform, this phenotype would be amenable to (semi)high-throughput screening to test compounds that correct mutant TAU–mediated neurite outgrowth abnormalities. This model might help to understand the role of TAU in neurite outgrowth, branching, or synapse formation and be potentially useful to test compounds aiming to correct the observed phenotype.

TAU aggregation is the pathological hallmark that best correlates with the progression of AD. Although it is accepted that TAU aggregates are rather a cause than a consequence of neurodegeneration, the precise molecular mechanisms by which TAU pathology is triggered and progresses throughout brain areas are not yet well understood. It is hypothesized that interfering with TAU expression, aggregation, and/or clearance may be a potential strategy for treating AD and other tauopathies [30], highlighting the need for *in vitro* TAU aggregation assays. Both in animal models and *in vitro* assays, physiological levels of TAU expression do not lead to TAU aggregation and requires not only the addition of recombinant TAU (seeds) but also the expression of nonphysiological levels of TAU expression (e.g., by overexpression of P301L TAU) [20]. In the triple TAU-mutant iPSC neurons on DIV70, we observed TAU aggregation only by seeding with K18 fibrils and without TAU overexpression. Similarly, we also observed a fivefold increase in aggregation by simply overexpressing TAU and in the absence of k18 fibrils. Importantly, we observe that TAU aggregates detected in mutant neurons are hyperphosphorylated, in analogy with which occurs in the brain of patients with AD [3]. Taken together, our findings suggest that the triple *MAPT* mutation is sufficient to seed for TAU aggregation, with a signal that is directly proportional to the amount of monomeric TAU available within the cell. As the seeding potential of endogenously expressed TAU has never been observed in any other *in vitro* assay, we suggest that triple TAU-mutant neurons may be a more clinically relevant model to screen for drugs interfering with TAU aggregation and/or propagation.

We found, based on RNAseq, qRT-PCR, Western blots, and functional studies, that triple TAU-mutant neuronal progeny displayed considerably increased levels of oxidative stress, ER/UPR stress, and activation of inflammatory-related response marker genes, which were also associated with an increased number of apoptotic cells. TAU abnormalities have been reported to lead to mitochondrial dysfunction and increased oxidative stress [31]. In addition, genetic and biochemical studies have shown that the UPR is activated at early stages in tauopathy brains [32]. Thus, the triple *MAPT*-mutant iPSC neuronal progeny recreate the TAU-mediated activation of the oxidative stress, ER/UPR, and inflammatory pathways; possibly also representing targetable phenotypes.

Transcriptome analysis demonstrated significant decreases in the levels of genes involved in the glutamate signaling pathway and a shift toward the expression of genes involved in GABAergic signaling in the triple mutant-TAU cells. Dysfunction of TAU is believed to cause an impaired microtubule organization that affects synapse organization, which underlies neurotoxicity and neurodegeneration. In

and $\log_2$ fold change >1) between WT and TAU-mutant neurons at DIV70 (1490 genes) and DIV110 (1868 genes, green), 395 of which (red) were common at both stages. (C) Supervised clustering analysis of a selected list of cortical neuronal markers in normal and TAU-mutant iPSC progeny on DIV70 and DIV110. (D) Supervised clustering analysis for glutamatergic vs. GABAergic marker expression in WT and TAU-mutant iPSC progeny on DIV70 and DIV110. (E) Ingenuity pathway analysis (IPA) of the glutamate receptor signaling pathway between both cell types on DIV110 (red: highly expressed genes on WT cells; green: highly expressed genes on TAU-mutant neurons). (F) IPA analysis of the synaptic long-term potentiation (LTP) pathway in WT and TAU-mutant iPSC progeny on DIV 110 (red: highly expressed genes on WT cells; green: highly expressed genes on mutant neurons).

addition to this mechanism, accumulation of TAU within intact dendritic spines results in synaptic abnormalities, where it disrupts synaptic function by impairing glutamate receptor trafficking or synaptic anchoring [33]. Consistent with this notion, we also observed a downregulation of markers of LTP pathway in the mutant cells. LTP is a form of synaptic plasticity believed to be involved in memory formation required for learning and memory [34]. LTP deficits have been described mostly for amyloidogenic rather than TAU-mutant models of AD [35]. However, our results suggest that this phenomenon might also be linked to TAU-mediated pathogenesis and suggest that the triple *MAPT*-mutant model might be a good platform to interrogate TAU-based disease mechanisms.

Different studies have reported an abnormally enhanced electrophysiological activity in TAU-mutant animal models [36,37] and in tauopathy patient-derived neurons [21]. The mechanisms by which aberrant TAU causes neuronal hyperexcitability are not yet elucidated, but it is believed that this may contribute to neuronal dysfunction at the onset of AD [36]. In our study, co-cultures of iPSC-derived neurons with primary astrocytes in MEAs showed an increase in electrophysiological activity for TAU-mutant cells in comparison with WT. This result, in principle, appears contradictory with the transcriptome data indicating the prevalence of a GABAergic inhibitory phenotype within mutant cells. Nevertheless, during development, there is developmental shift in GABAergic populations from immature excitatory to mature inhibitory synaptic transmission [38]. Immature GABAergic neurons are not able to maintain a proper reversal potential for the ion chloride (Cl^-), resulting in a higher intracellular Cl^- concentration compared with mature neurons. This is because the chloride exporter KCC2 (*SLC12A5*) is not yet expressed in immature GABAergic neurons. After GABA synaptic transmission, this deregulated Cl^- potential results into an outward Cl^- flux and hence, an activating depolarization [39]. We therefore queried the RNAseq data and found that the expression of KCC2 (*SLC12A5*) was substantially decreased in mutant neurons compared with WT cells mainly at later stages (DIV110, Supplementary Fig. 5G), reconciling the observation of a higher electrophysiological activity with a predominant GABAergic phenotype within TAU-mutant neurons. Recently, it has been described that amyloid precursor protein deficiency leads to KCC2 degradation, causing impaired chloride concentrations inside the neurons. This resulted in deficient GABAergic inhibition in the hippocampus of patients with AD [40]. Our results might suggest a role for aberrant TAU as well in this phenomenon.

The increased electrophysiological activity of TAU-mutant cells in MEAs was not reproduced in whole cell patch-clamps experiments. Possible explanations for this might be as follows: (1) considerable fewer neurons are sampled in patch-clamp studies compared with MEA analysis; (2) MEA experiments allow to determine neuronal network signaling, in contrast to patch-clamp where only individual cell electrophysiological activities can be evaluated; and (3) astrocytes are essential to support neuronal activity both *in vivo* and *in vitro* and the absence of astrocytes in the patch-clamp experiments might have had a negative impact on the neuronal activity assessed [22].

Finally, we found defective cortical maturation *in vitro* from triple TAU-mutant cells, with a notable impairment in the capacity to differentiate toward $SATB2^+$ superficial cortical layer neurons and a relative increase in cells with deeper cortical layer markers. Concomitantly, we observed a decreased frequency of *TBR1*-positive cells, a transcription factor governing cortical layer formation with altered expression in patients with AD [23]. Decreased cortical neurogenesis have been described as well for haploinsufficient progranulin mutant neuronal progeny derived from iPSCs of frontotemporal dementia patients [41], which might suggest that aberrant mechanisms convey in similar neurodegenerative consequences. The reason for the failure to generate superficial layer cortical neurons observed in triple TAU-mutant neurons is not clear, but one possibility is that these cells might be more sensitive to (oxidative, ER/UPR, and/or inflammatory) stress, as has been reported in patients with AD [42], with therefore a more specific disappearance of these cells from the culture. The loss of the predominantly glutamatergic superficial layer neurons would result in an imbalance of excitatory vs. inhibitory signaling [43], as we have observed at the transcriptome level in our cultures.

In conclusion, we generated a hiPSC-derived TAU-mutant model that reproduces key several neurodegenerative phenotypes associated with tauopathies, such as altered TAU expression, including phosphorylated isoforms, TAU aggregation, defective neurite conformation, altered neuronal maturation, enhanced electrophysiological excitability, and upregulation of stress pathways. The robustness of the footprint-free and nonadditional mutation-generated line, together with the advantages inherent to iPSC-derived systems, makes the generated model an ideal candidate platform for the identification of therapeutic targets counteracting TAU pathology excluding the variability associated with patient-derived cells.

4. Experimental procedures

4.1. Human iPSC lines culture conditions, gene editing, and selection

The hiPSC ChiPS6b healthy donor-derived WT cells (purchased from Takara Bio Inc.) were maintained in feeder-free conditions using E8 medium (Life Technologies) on hESC-qualified matrigel (Becton Dickinson) and were split twice a week using EDTA (Lonza). Q6

4.2. Selection of TAU mutations

We aimed to generate a cell model that reproduces several aspects of tauopathy-related neurodegeneration. Therefore, we selected the N279K, P301L, and E10+16 mutations

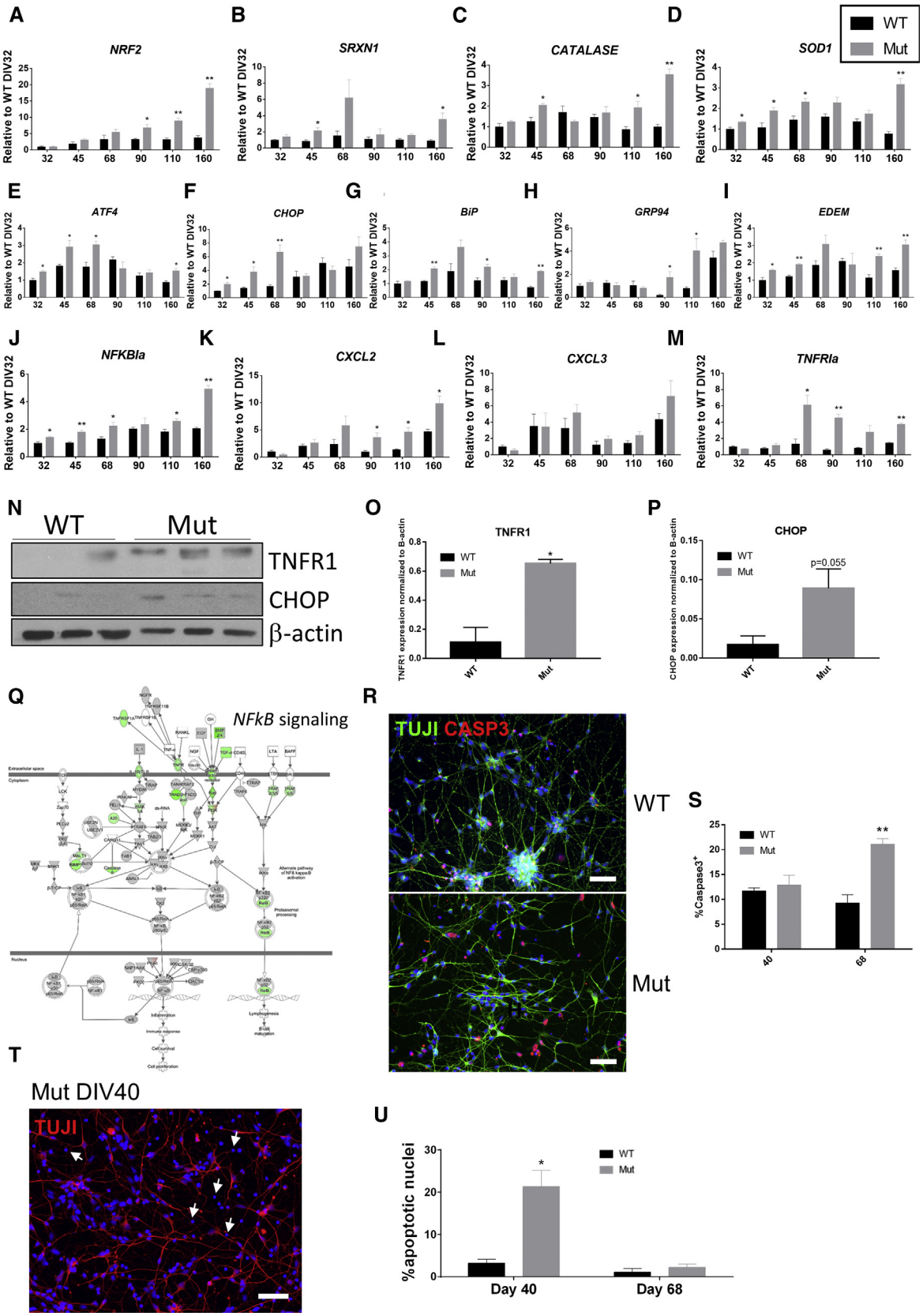

Fig. 6. qRT-PCR confirms increased stress pathway gene expression in TAU-mutant cortical progeny. (A–M) qRT-PCR analysis for genes implicated in oxidative stress (A–D), ER/UPR stress (E–I), and inflammatory responses (WT: black and TAU-mutant iPSC: gray, J–M). Gene expression levels are shown as fold changes relative to WT NPCs on DIV32 (gene expression was normalized to the housekeeping gene *GAPDH*). (N–P) Western blot experiments and

present within the exon 10 or next intron of the *MAPT* gene. These three mutations are the most prevalent in FTDP-17, accounting for up to 60% of all cases [16]. Presence of the N279K or P301L mutations causes early onset and aggressive disease course, increased TAU-phosphorylated species both in neurons and glia, and a higher prevalence of the pathogenic 4R TAU isoforms, altering the 3R/4R ratio [14]. The E10+16 mutation is located in the intron between exons 10 and 11, causing alterations in the stem-loop structure and affecting splicing capacity of pre-mRNA, with increased exon 10 incorporation as a result and, therefore, a higher expression of the 4R TAU isoforms [15].

4.3. Design of gene-editing strategy

To accurately and efficiently target the exon 10 of the *MAPT* gene, we developed a combination of specific targeting using CRISPR-FokI nucleases [17] together with the construction of a template DNA vector harboring the three selected mutations and a dual HYG^R (positive)/TK (negative) selection cassette (backbone vector provided by Dr. Kosuke Yusa, Wellcome Trust Sanger Institute, UK [18]). This template incorporated as well a 700 bp left and right homology arms to allow homologous recombination of the DNA template into the genome, which should result, in most cases, in the incorporation of the three selected mutations. To generate footprint-free mutant cell lines, we combined this strategy with the use of the piggyBac transposase technology, which allows excision by recombining TTAA sequences contained in their integration sites (inverted terminal repeats) [44]. Therefore, we introduced the selection cassette next to an endogenous TTAA sequence, such that following cassette excision the TTAA remained, without altering the genomic sequence, therefore generating cell lines without any additional genetic alterations [18]. CRISPR-FokI nucleases were designed using the Zinc Finger Consortium (ZiFiT) algorithm [45] covering the target sequence. Target site 1: TTATTAATTATCTGCACCTT, target site 2: AGCAACGTCCAGTCCAAGTG. The efficiency of the selected nucleases was tested and validated on HEK293T cells (not shown).

4.4. Nucleofection and selection

Nucleofection was performed as previously described [46]. Briefly, two million hiPSCs were transfected with 5 μg donor vector, 3 μg of pSQT1601 plasmid encoding for dCas9-FokI and 1 μg of each plasmid encoding for gRNAs directed toward left and right target sites using the Amaxa Nucleofector, and the hESC Nucleofector Solution Kit 2 (Amaxa, Lonza) using the program F16. Cells were cultured in feeder-free conditions as previously described in the presence of a ROCK inhibitor analog (Revitacell®, Life Technologies). Selection was initiated after 2–3 days with 25–50 mg/mL of Hygromycin B (Sigma-Aldrich) and maintained for 10–15 days. Recombinant colonies were manually picked and expanded for further characterization.

Removal of the selection cassette from selected clones was performed by nucleofection of 5 μg of the PiggyBac Transposon. Two to 3 days after the transfection, cells were treated with 0.5 μM 1-(2-deoxy-2-fluoro-beta-D-arabinofuranosyl)-5-iodouracil (FIAU) for 7 days. GFP expression was monitored by immunofluorescence and FACS during the selection process with both HYG and FIAU. Q7

4.5. Flow cytometry

To determine the frequency of GFP^+ cells during the initial HYG and subsequent FIAU selection procedure, cells were enzymatically harvested using accutase, centrifuged, and resuspended in 100 μL FACS buffer (PBS 1×, 2% fetal bovine serum and 0.02% sodium azide). Cells were analyzed on a FACSCanto flow cytometer using the FACS DIVA software (Becton & Dickinson). After exclusion of cell doublets, GFP fluorescence was determined on FL1-FITC channel, with gates established based on fluorescence of untargeted (WT) cells.

All results were analyzed using Flow Jo (FlowJo, LLC, USA) and FACS DIVA software (Becton & Dickinson). Flow cytometry and FACS sorting was performed at the KU Leuven Flow Cytometry Facility.

4.6. PCR genotyping

PCR genotyping was done using 40 ng of genomic DNA with Go Taq DNA polymerase (Promega) in 10 μL reactions. Primer sequences and PCR program conditions are described in Supplementary Table 1. PCR products were loaded on 1.5% agarose (Sigma) gels and visualized with SYBR Safe (Invitrogen) on a Gel Doc XR+ System (Bio-Rad).

4.7. Pluripotency characterization

Both WT and triple TAU-mutant cells were subjected to spontaneous differentiation mediated by embryoid body formation and subsequently analyzed for the three-lineage

quantification of protein levels for the inflammatory response (tumor necrosis factor receptor 1 (TNFR1)) and ER/UPR stress (CHOP) markers respectively, on DIV65. (Q) IPA analysis, based on RNA-seq analysis depicted in Fig. 5, of the NFkB signaling pathway (red: highly expressed genes on WT cells; green: highly expressed genes on TAU-mutant neurons). (R and S) Representative immunostaining images and quantification on DIV40 and DIV68 of WT and TAU-mutant cells stained with antibodies against activated CASPASE3 and TUJ1. (T–U) Analysis of apoptotic nuclei in WT and TAU-mutant cortical neuron progeny on DIV40 and DIV68 (a representative picture of TAU-mutant neurons at DIV40 is shown for immunostaining with TUJI antibodies and Hoechst). Apoptotic nuclei were defined as those nuclei with smaller size and more concentrated Hoechst signal, lacking expression of TUJI. Representative images of N = 3–4 independent differentiations. Hoechst 33258 (blue) was used as nuclear marker. Scale bar: 50 μm. Data are represented as mean ± SEM of N = 3–4 independent experiments. $*P < .05$, $**P < .01$.

differentiation using the ScoreCard methodology [47] (Thermo Fisher Scientific), according to manufacturer instructions.

4.8. Neuronal differentiation protocol

Cortical neurons were generated from both WT and triple TAU mutant hiPSCs as previously described by Shi et al. [19]. Briefly, single-cell hiPSCs were collected and plated on Matrigel-coated (BD) well plates in E8 medium supplemented with ROCK inhibitor analog (Revitacell, Life Technologies). Once the cell culture reached 95% confluence, neural induction was initiated by changing the culture medium to N2B27 medium, consisting of a 1:1 mixture of N2- and B27-containing media. N2 medium consisted of DMEM/F12, N2, 5 μg/mL insulin, 1× GlutaMax, 1× nonessential amino acids, 1× 2-mercaptoethanol, 1× penicillin/streptomycin. B27 medium consisted of Neurobasal, B27 without retinoic acid, 1× glutamax, 1 × 200 mM glutamine and 1× penicillin/streptomycin (all from Life Technologies). N2B27 medium was supplemented with the small molecules SB431542 10 μM (Tocris) and LDN193189 1 μM (Miltenyi Biotec), and daily medium changes were performed till day 12. Then, neuroepithelial cells were collected by dissociation with dispase and replated in N2B27 medium, including 20 ng/μL bFGF (Peprotech) on matrigel-coated dishes. Rosette-forming neuroepithelial cells were purified two more times (one each after 4–5 days), after which single-cell splitting with accutase was performed twice before cryopreserving NPCs (which occurred on DIV32–33). For terminal neuronal differentiation, NPCs were thawed, cultured in N2B27 medium for a few days, and replated on DIV40-42 at 15–25.000 cells per cm^2 on poly-ornithine and laminin-coated plastic dishes in N2B27 medium and maintained for up to DIV200 with partial medium changes twice a week.

4.9. RNA extraction, cDNA synthesis, and gene expression (QPCR)

Total RNA was purified using the GenElute™ Mammalian Total RNA Miniprep Kit (Sigma-Aldrich, Saint Louis, MO, USA) and ZR RNA MicroPrep (Zymo Research, CA, USA). After concentration and integrity validation (NanoDrop 1000, Thermo Fisher Scientific, MA USA), cDNA was generated using 0.5–1 μg of RNA with SuperScript® III First-Strand Synthesis SuperMix for qRT-PCR kit (Invitrogen, CA, USA), and qRT-PCR was performed in technical triplicates on a ViiA™ 7 Real-Time PCR System with 384-well plate (Applied Biosystems, Carlsbad, CA, USA) with a Platinum® SYBR® Green qPCR SuperMix-UDG w/ROX (Invitrogen, CA, USA) and primers mix at final concentration of 250 nM.

Gene expression (cycle threshold) values were normalized based on the *GAPDH* (glyceraldehyde 3-phosphate dehydrogenase) housekeeping gene, and the delta CT calculated. Gene-specific primers were designed in exon-exon spanning regions in common domains of all isoforms described for a given gene. The efficiency of primers was tested by serial dilutions of cDNA and by calculating the coefficient of regression (R^2). An efficiency of 90%–105% with an $R^2 \geq 95\%$ was accepted. See Supplementary Table 2 for a list of all qRT-PCR primers used in this study.

Identification of the 3R or 4R species was done using the following TaqMan assays (Thermofisher): glyceraldehyde 3-phosphate dehydrogenase (Hs99999905_m1), *MAPT* all isoforms (Hs00902194_m1), *MAPT 3R* isoforms (Hs00902192_m1), and *MAPT 4R* isoforms (Hs00902312_m1).

4.10. Transcriptome analysis by RNA sequencing

Total RNA was purified using the GenElute™ Mammalian Total RNA Miniprep Kit (Sigma). RNA concentration and purity were determined spectrophotometrically using the NanoDrop ND-1000 (NanoDrop Technologies), and RNA integrity was assessed using a Bioanalyzer 2100 (Agilent). Per sample, an amount of 100 ng of total RNA was used as input. Using the Illumina TruSeq® Stranded mRNA Sample Prep Kit (protocol 15031047 Rev.E "October 2013"), poly-A–containing mRNA molecules were purified from the total RNA input using poly-T oligo-attached magnetic beads. In a reverse transcription reaction using random primers, RNA was converted into first strand cDNA and subsequently converted into double-stranded cDNA in a second strand cDNA synthesis reaction using DNA Polymerase I and RNAse H. The cDNA fragments were extended with a single deoxyadenosine to the 3′ ends of the blunt-ended cDNA fragments after which multiple indexing adapters were ligated, introducing different barcodes for each sample. Finally, enrichment PCR was carried out to enrich DNA fragments that had adapter molecules on both ends and to amplify the DNA in the library. Sequence libraries of each sample were equimolar pooled and sequenced on an Illumina NextSeq 500 instrument (High Output, 75 bp, Single Reads, v2) at the VIB Nucleomics core (www.nucleomics.be).

Low-quality ends and adapter sequences were trimmed off from the Illumina reads. Subsequently, small reads (length < 35 bp), ambiguous reads (containing N), and low-quality reads (more than 50% of the bases < Q25) were filtered. Processed reads were aligned with Tophat, v2.0.8b, to the human reference genome (GRCh38), as downloaded from the Genome Reference Consortium (https://www.ncbi.nlm.nih.gov/grc/human/data). Default Tophat parameter settings were used, except for "min-intron-length = 50", "max-intron-length = 500,000", "no coverage-search" and "read-realign-edit-dist = 3".

Principal component analysis and volcano plots were generated in the statistical software R, version 3.4.1. Clustering was performed with ClustVis [48]. Differentially expressed genes were identified based on $P > .05$, and a fold

change of two or more in gene expression among the different pair-wise comparison was used to identify the differentially expressed genes. Gene ontology of the different differentially expressed genes was carried out using the Gene Ontology Consortium (http://www.geneontology.org/). Ingenuity pathway analysis was performed with build 456367, content version 39480507.

4.11. Western blot

Cells were lysed and sonicated in RIPA buffer (Sigma), containing phosphatase and protease inhibitors. Lysate was cleared by 15 min centrifugation at 12,000× *g*, and supernatant was recovered for protein quantification. Twenty micrograms of protein extract was then loaded per lane and resolved on SDS-PAGE before transferring to nitrocellulose membranes. Blocking was done for 1 h with 5% nonfat milk solution in PBST before incubation with primary antibodies.

For TAU WBs, cells were lysed in RIPA buffer (150 mM NaCl, 50 mM Tris-HCl (pH 7.5), 150 mM NaCl, 1 mM EDTA, 1% NP-40, 0.25% sodium deoxycholate supplemented with complete protease inhibitors (Roche) and PhosSTOP (Sigma). The homogenate was ultra-centrifuged at 100,000× *g* for 60 min at 4°C. Equal amounts of protein were taken and analyzed by SDS–PAGE and semi-quantitative Western immunoblot. Bands were visualized using a cooled charge-coupled device camera (ImageQuant LAS-4000; GE Healthcare) and quantified by AIDA Image Analyzer software.

5. AlphaLISA immunoassay

Cell lysis was performed using RIPA buffer containing phosphatase (PhosSTOP, Roche, Mannheim, Germany) and protease inhibitors (cOmplete, Roche) in culture plates for 1 h at room temperature (RT) on an orbital shaker. For hTAU10/hTAU10 TAU aggregation assays, we performed measurements in duplicates using 5 µL of lysate each time. Five microliters of the remaining lysate were used for the relative quantification of total TAU and for measuring cell viability, respectively. Each sample was transferred to a 384-well assay plate for AlphaLISA reaction, in which 5 µL of cell extracts were incubated for 2 h at RT with a mixture of biotinylated antibody and acceptor beads. Subsequently, donor beads were added to the wells and incubated at RT for 30 min before reading at 615 nm (on illumination at 680 nm) on the EnVision plate reader (PerkinElmer, Waltham, MA). Output measurement is quantified as relative fluorescent units and compared versus control conditions.

5.1. Immunostainings

Cells were washed with PBS 1× and fixed for 15 min at RT with 4% formaldehyde solution and washed with PBS. Preparations were permeabilized in 0.1% Triton-X-100 (Sigma) and blocked in 10% donkey or goat serum (Dako) in PBS for 1 h at RT. Primary antibodies were incubated overnight at 4°C in 5% in donkey or goat serum in PBS, washed 3 times, and incubated for 1 h at RT with fluorescently labeled secondary antibodies diluted to 1:500. Samples were incubated for 15 min at RT with Hoechst 33258 (1:2000 dilution) for nuclear staining and mounted with ProLong® Gold Antifade Mountant (Thermo Fisher Scientific). The list of primary and secondary antibodies and the dilutions used can be found in Supplementary Tables 3 and 4.

5.2. Image acquisition and analysis

The stained cells were examined using an Axioimager.Z1 microscope (Carl Zeiss). For quantification purposes, at least five independent fields per condition and per experiment were obtained. For neurite outgrowth experiments, images were acquired on an In Cell Analyzer 2000 High Content Imager (GE Healthcare), acquiring sufficient numbers of images to cover at least 70% of the well area. Data analysis was performed using the In Cell image analysis software (GE Healthcare), with the specific software package of neurite outgrowth.

5.3. EdU incorporation assays

Cells were pulse-labeled with 10 µM 5-ethynyl-2′-deoxyuridine (EdU, Life Technologies) for 3 hours, and several medium washes were performed afterward. Twenty-four hours after onset of EdU incubation, cells were fixed with 4% PFA for 15 minutes, washed with PBS + 2% BSA, followed by 30′ permeabilization with PBS + 0.5% Triton. Cells were then incubated for 30 min at RT with freshly prepared reaction buffer (per mL: 976 µL PBS + 10 µL $CuSO_4$ + 10 µL Sodium Ascorbic + 4 µL of 1/100 Azide-AF647 antibody), washed for three times, and stained with β-3-tubulin and Hoechst. The presence of EdU+ cells was evaluated using an Axioimager.Z1 microscope (Carl Zeiss).

5.4. Electrophysiological recordings

Whole-cell patch-clamp recordings of hIPSC-derived cortical neurons were carried out in a recording chamber which was continuously perfused with artificial cerebrospinal fluid at RT. Artificial cerebrospinal fluid contained 145 mM NaCl, 5 mM KCl, 2 mM $CaCl_2$, 2 mM $MgCl_2$, 10 mM Hepes, and 12 mM glucose (pH adjusted to 7.4 with NaOH; ~310 mOsm). Cells were visualized by an inverted Olympus IX73 microscope equipped with a 40× objective. Recording patch pipettes were pulled from borosilicate glass using a vertical PIP6 micropipette puller (HEKA Elektronik, Lambrecht/Pfalz, Germany) and filled with an internal solution containing (in mM): 120 K-gluconate, 20 KCl, 1 $MgCl_2$, 10 Hepes, 0.2 EGTA, 0.3 Na-GTP, 5 NaCl, 4 Mg-ATP (pH adjusted to 7.3 with KOH; ~290 mOsm). Current-clamp mode was applied to measure action potentials, while voltage-gated Na+ and K+ currents were recorded in voltage-clamp mode. An online P4 leak

subtraction protocol was applied during the acquisition of all voltage-gated currents. Details of the performed current- and voltage-clamp protocols are described in the results section. Signals were acquired, filtered (at 2.8 kHz), and digitized (at 20 kHz) using an EPC10 USB amplifier and PatchMaster software (HEKA Elektronik). The liquid junction potential of 14 mV was corrected off-line. Action potential detection was performed using Stimfit software; current amplitudes were measured by PatchMaster software.

5.5. Multi-electrode arrays

Human iPSC-derived NPCs (DIV30) were co-cultured with rat primary astrocytes in 1:1 ratio and plated onto 48-well MEA plates (Axion BioSystems) coated with polyethyleneimine and laminin. Plating was done using drop seeding method, where 15 μL of mixed cells (60,000 cells in total) in a 10% dilution of N2B27media: Matrigel (BD Biosciences, Cat#356230) was placed onto each well. Cells were then cultured in neuronal differentiation media for up to 40 additional days (DIV70), with partial medium replacements every 2–3 days. Spontaneous network activity of the maturating neurons was recorded for 5 minutes on specific time points using the Axion Biosystems Maestro MEA at 37°C and 5% CO_2.

Data analysis was performed using AxIs software (Axion Biosystems) to obtain from the recording the data concerning the spikes, bursts, and network activity. Quality criteria for the assays were defined as follows: active electrodes were defined as an electrode having an average of more than five spikes per minute. Wells in which less than 30% of electrodes were active were considered inactive and removed from analysis. For synchronous network activity, at least 25% of the total electrode in a well was required to participate in a network event in order for the network to be qualified as network spike or bursts.

5.6. Statistical analysis

Comparisons between two groups were analyzed using unpaired or paired two-tailed Student's t test. *P*-values $< .05$ were considered significant (*). Data are shown as mean, and error bars represent standard error of mean of a minimum three independent experiments.

For patch-clamp data, a Mann-Whitney test or a Kruskal-Wallis with post hoc Dunn's multiple comparison's test were used to compare respectively two or three groups as patch clamp data were not normally distributed. Results were plotted and analyzed using GraphPad Prism 6 software.

Acknowledgments

The authors would like to thank all members of the Stellar project consortium for fruitful scientific discussions and collaborations.

The authors would like to thank Prof. F.L. and Anchel De-Jaime (Stem Cell Institute, KU Leuven) for their assistance with Western blotting of stress marker proteins.

J.A.G.L. has been supported by a fellowship from Alfonso Martín Escudero Foundation (Madrid, Spain). P.V.D. holds a senior clinical investigatorship of FWO-Vlaanderen. The work was supported by the Stellar project iPSC-NeDi (Janssen Pharmaceutica), IWT-iPSCAF grant (#150031), IWT-VIND project and the KUL-PF Stem Cells (#PFO3) to C.M.V.

Authors' contributions: C.M.V. and A.E. conceived the study. J.A.G.L. and C.M.V. designed the project and experiments. J.A.G.L. performed most of the experiments and performed analysis of the data. A.C.S. provided expertise and performed TAU aggregation, MEAs, and some WB experiments and actively contributed to the writing of the manuscript. K.E. actively assisted and performed neuronal differentiations and immunostainings. A.S. performed patch-clamp experiments and analysis. J.T. assisted with neurite outgrowth and transcriptome analysis. R.F. and A.Q. helped with gene-editing and iPSC maintenance. L.O. and A.N. helped with the gene-editing strategy. K.W. assisted with electrophysiology experiments and data interpretation. L.S. performed WBs for TAU protein isoforms. A.S. and B.D.S. assisted with data interpretation. M.K. and F.P. assisted with MEAs experiments. P.V.D. provided support for electrophysiology experiments. L.T. performed most of the transcriptome data. J.A.G.L., and C.M.V. wrote the manuscript. C.M.V. provided scientific guidance and support. All the authors have read the manuscript.

Supplementary data

Supplementary data related to this article can be found at https://doi.org/10.1016/j.jalz.2018.05.007.

RESEARCH IN CONTEXT Q15

1. Systematic review: ■■■.
2. Interpretation: ■■■.
3. Future directions: ■■■.

References

[1] Spillantini MG, Goedert M. Tau protein pathology in neurodegenerative diseases. Trends Neurosci 1998;21:428–33.
[2] Jack CR Jr, Holtzman DM. Biomarker modeling of Alzheimer's disease. Neuron 2013;80:1347–58.
[3] Goedert M, Spillantini MG, Jakes R, Rutherford D, Crowther RA. Multiple isoforms of human microtubule-associated protein tau:

sequences and localization in neurofibrillary tangles of Alzheimer's disease. Neuron 1989;3:519–26.
[4] Goedert M, Crowther RA, Spillantini MG. Tau mutations cause frontotemporal dementias. Neuron 1998;21:955–8.
[5] Goedert M, Ghetti B, Spillantini MG. Frontotemporal dementia: implications for understanding Alzheimer disease. Cold Spring Harb Perspect Med 2012;2:a006254.
[6] Rossi G, Tagliavini F. Frontotemporal lobar degeneration: old knowledge and new insight into the pathogenetic mechanisms of tau mutations. Front Aging Neurosci 2015;7:192.
[7] D'Souza I, Poorkaj P, Hong M, Nochlin D, Lee VM, Bird TD, et al. Missense and silent tau gene mutations cause frontotemporal dementia with parkinsonism-chromosome 17 type, by affecting multiple alternative RNA splicing regulatory elements. Proc Natl Acad Sci U S A 1999;96:5598–603.
[8] Guerrero-Muñoz MJ, Gerson J, Castillo-Carranza DL. Tau oligomers: the toxic player at synapses in Alzheimer's disease. Front Cell Neurosci 2015;9:464.
[9] Götz J, Deters N, Doldissen A, Bokhari L, Ke Y, Wiesner A, et al. A decade of tau transgenic animal models and beyond. Brain Pathol 2007;17:91–103.
[10] Fong H, Wang C, Knoferle J, Walker D, Balestra ME, Tong LM, et al. Genetic correction of tauopathy phenotypes in neurons derived from human induced pluripotent stem cells. Stem Cell Reports 2013; 1:226–34.
[11] Ehrlich M, Hallmann AL, Reinhardt P, Araúzo-Bravo MJ, Korr S, Röpke A, et al. Distinct neurodegenerative changes in an induced pluripotent stem cell model of frontotemporal dementia linked to mutant TAU protein. Stem Cell Reports 2015;5:83–96.
[12] Wren MC, Zhao J, Liu CC, Murray ME, Atagi Y, Davis MD, et al. Frontotemporal dementia-associated N279K tau mutant disrupts subcellular vesicle trafficking and induces cellular stress in iPSC-derived neural stem cells. Mol Neurodegener 2015;10:46.
[13] Imamura K, Sahara N, Kanaan NM, Tsukita K, Kondo T, Kutoku Y, et al. Calcium dysregulation contributes to neurodegeneration in FTLD patient iPSC-derived neurons. Sci Rep 2016;6:34904.
[14] Delisle MB, Murrell JR, Richardson R, Trofatter JA, Rascol O, Soulages X, et al. A mutation at codon 279 (N279K) in exon 10 of the Tau gene causes a tauopathy with dementia and supranuclear palsy. Acta Neuropathol 1999;98:62–77.
[15] Hutton M, Lendon CL, Rizzu P, Baker M, Froelich S, Houlden H, et al. Association of missense and 5'-splice-site mutations in tau with the inherited dementia FTDP-17. Nature 1998;393:702–5.
[16] Arendt T, Stieler JT, Holzer M. Tau and tauopathies. Brain Res Bull 2016;126:238–92.
[17] Tsai SQ, Wyvekens N, Khayter C, Foden JA, Thapar V, Reyon D, et al. Dimeric CRISPR RNA-guided FokI nucleases for highly specific genome editing. Nat Biotechnol 2014;32:569–76.
[18] Yusa K. Seamless genome editing in human pluripotent stem cells using custom endonuclease-based gene targeting and the piggyBac transposon. Nat Protoc 2013;8:2061–78.
[19] Shi Y, Kirwan P, Livesey FJ. Directed differentiation of human pluripotent stem cells to cerebral cortex neurons and neural networks. Nat Protoc 2012;7:1836–46.
[20] Medda X, Mertens L, Versweyveld S, Diels A, Barnham L, Bretteville A, et al. Development of a scalable, high-throughput-compatible assay to detect tau aggregates using iPSC-derived cortical neurons maintained in a three-dimensional culture format. J Biomol Screen 2016;21:804–15.
[21] Iovino M, Agathou S, González-Rueda A, Del Castillo Velasco-Herrera M, Borroni B, Alberici A, et al. Early maturation and distinct tau pathology in induced pluripotent stem cell-derived neurons from patients with MAPT mutations. Brain 2015;138:3345–59.
[22] Qi Y, Zhang XJ, Renier N, Wu Z, Atkin T, Sun Z, et al. Combined small-molecule inhibition accelerates the derivation of functional cortical neurons from human pluripotent stem cells. Nat Biotechnol 2017;35:154–63.
[23] Bedogni F, Hodge RD, Elsen GE, Nelson BR, Daza RA, Beyer RP, et al. Tbr1 regulates regional and laminar identity of postmitotic neurons in developing neocortex. Proc Natl Acad Sci U S A 2010; 107:13129–34.
[24] Anderson S, Vanderhaeghen P. Cortical neurogenesis from pluripotent stem cells: complexity emerging from simplicity. Curr Opin Neurobiol 2014;27:151–7.
[25] Johnson K, Barragan J, Bashiruddin S, Smith CJ, Tyrrell C, Parsons MJ, et al. Gfap-positive radial glial cells are an essential progenitor population for later-born neurons and glia in the zebrafish spinal cord. Glia 2016;64:1170–89.
[26] Alavi Naini SM, Soussi-Yanicostas N. Tau hyperphosphorylation and oxidative stress, a critical vicious circle in neurodegenerative tauopathies? Oxid Med Cell Longev 2015;2015:151979.
[27] Guo T, Noble W, Hanger DP. Roles of tau protein in health and disease. Acta Neuropathol 2017;133:665–704.
[28] Espuny-Camacho I, Arranz AM, Fiers M, Snellinx A, Ando K, Munck S, et al. Hallmarks of Alzheimer's disease in stem-cell-derived human neurons transplanted into mouse brain. Neuron 2017;93:1066–1081.e8.
[29] Majounie E, Cross W, Newsway V, Dillman A, Vandrovcova J, Morris CM, et al. Variation in tau isoform expression in different brain regions and disease states. Neurobiol Aging 2013;34:1922.e7. 1922.e12.
[30] Brunden KR, Trojanowski JQ, Lee VM. Advances in tau-focused drug discovery for Alzheimer's disease and related tauopathies. Nat Rev Drug Discov 2009;8:783–93.
[31] Rodríguez-Martín T, Pooler AM, Lau DHW, Mórotz GM, De Vos KJ, Gilley J, et al. Reduced number of axonal mitochondria and tau hyperphosphorylation in mouse P301L tau knockin neurons. Neurobiol Dis 2016;85:1–10.
[32] Nijholt DA, van Haastert ES, Rozemuller AJ, Scheper W, Hoozemans JJ. The unfolded protein response is associated with early tau pathology in the hippocampus of tauopathies. J Pathol 2012; 226:693–702.
[33] Hoover BR, Reed MN, Su J, Penrod RD, Kotilinek LA, Grant MK, et al. Tau mislocalization to dendritic spines mediates synaptic dysfunction independently of neurodegeneration. Neuron 2010; 68:1067–81.
[34] Van der Jeugd A, Ahmed T, Burnouf S, Belarbi K, Hamdame M, Grosjean ME, et al. Hippocampal tauopathy in tau transgenic mice coincides with impaired hippocampus-dependent learning and memory, and attenuated late-phase long-term depression of synaptic transmission. Neurobiol Learn Mem 2011;95:296–304.
[35] Lo AC, Iscru E, Blum D, Tesseur I, Callaerts-Vegh Z, Buée L, et al. Amyloid and tau neuropathology differentially affect prefrontal synaptic plasticity and cognitive performance in mouse models of Alzheimer's disease. J Alzheimers Dis 2013;37:109–25.
[36] Hall AM, Throesch BT, Buckingham SC, Markwardt SJ, Peng Y, Wang Q, et al. Tau-dependent Kv4.2 depletion and dendritic hyperexcitability in a mouse model of Alzheimer's disease. J Neurosci 2015; 35:6221–30. Q12
[37] Crimins JL, Rocher AB, Luebke JI. Electrophysiological changes precede morphological changes to frontal cortical pyramidal neurons in the rTg4510 mouse model of progressive tauopathy. Acta Neuropathol 2012;124:777–95.
[38] Ben-Ari Y. Excitatory actions of gaba during development: the nature of the nurture. Nat Rev Neurosci 2002;3:728–39.
[39] Ben-Ari Y, Cherubini E, Corradetti R, Gaiarsa JL. Giant synaptic potentials in immature rat CA3 hippocampal neurones. J Physiol 1989; 416:303–25.
[40] Chen M, Wang J, Jiang J, Zheng X, Justice NJ, Wang K, et al. APP modulates KCC2 expression and function in hippocampal GABAergic inhibition. Elife 2017;6:e20142.
[41] Raitano S, Ordovàs L, De Muynck L, Guo W, Espuny-Camacho I, Geraerts M, et al. Restoration of progranulin expression rescues cortical neuron generation in an induced pluripotent stem cell model of frontotemporal dementia. Stem Cell Reports 2015;4:16–24.

[42] Romito-DiGiacomo RR, Menegay H, Cicero SA, Herrup K. Effects of Alzheimer's disease on different cortical layers: the role of intrinsic differences in Abeta susceptibility. J Neurosci 2007;27:8496–504.
[43] Fang WQ, Chen WW, Jiang L, Liu K, Yung WH, Fu AK, et al. Overproduction of upper-layer neurons in the neocortex leads to autism-like features in mice. Cell Rep 2014;9:1635–43.
[44] Yusa K, Rad R, Takeda J, Bradley A. Generation of transgene-free induced pluripotent mouse stem cells by the piggyBac transposon. Nat Methods 2009;6:363–9.
[45] Sander JD, Maeder ML, Reyon D, Voytas DF, Joung JK, Dobbs D. ZiFiT (Zinc Finger Targeter): an updated zinc finger engineering tool. Nucleic Acids Res 2010;38:W462–8.
[46] Ordovás L, Boon R, Pistoni M, Chen Y, Wolfs E, Guo W, et al. Efficient recombinase-mediated cassette exchange in hPSCs to study the hepatocyte lineage reveals AAVS1 locus-mediated transgene inhibition. Stem Cell Rep 2015;5:918–31.
[47] Bock C, Kiskinis E, Verstappen G, Gu H, Boulting G, Smith ZD, et al. Reference Maps of human ES and iPS cell variation enable high-throughput characterization of pluripotent cell lines. Cell 2011;144:439–52.
[48] Metsalu T, Vilo J. ClustVis: a web tool for visualizing clustering of multivariate data using Principal Component Analysis and heatmap. Nucleic Acids Res 2015;43:W566–70.